Robotica (2024), **42**, pp. 72–86
doi:10.1017/S0263574723001340

CAMBRIDGE UNIVERSITY PRESS

RESEARCH ARTICLE

Modeling and optimization of motion for inchworm-inspired magnetically driven soft robot

Yue Di[1], Yuyan Zhang[1,2], Yintang Wen[1,2] and Yaxue Ren[1]

[1]School of Electrical Engineering, Yanshan University, Qinhuangdao, Hebei, 066004, China and [2]Key Lab of Measurement Technology and Instrumentation of Hebei Province, Yanshan University, Qinhuangdao, Hebei, 066004, China
Corresponding author: Yuyan Zhang; Email: yyzhang@ysu.edu.cn

Received: 24 March 2023; **Revised:** 6 August 2023; **Accepted:** 5 September 2023; **First published online:** 18 October 2023

Keywords: inchworm inspired; soft robot; motion model; magnetic drive; structure optimization

Abstract

At present, the research of soft crawling robot pays more attention to the material manufacturing, but neglects the robot modeling. The high degree of freedom of the soft crawling robot makes it more difficult to establish its motion model and analyzes its motion performance. The centimeter-level wireless driven soft crawling robot has great advantages and application scenarios in narrow space exploration. Therefore, this paper proposed a soft robot driven by magnetism to crawling inchworm. By studying the crawling behavior of inchworm and the characteristics of flexible materials driven by magnetism, the structure of the soft robot was designed and the motion model of inchworm was established. The motion model is analyzed and simulated, the structure size of the robot is optimized, and the effectiveness of the model is verified by experiments. The robot's crawling motion is realized by coupling the structure of the robot's torso and legs with the flexible magnetic film. Driven by the alternating magnetic field, the maximum motion speed of the robot is 28.24 mm/s. At the same time, the robot can also move in narrow space such as pipes, which can satisfy the centimeter-level space detection and ensure the high efficiency, providing a new idea for narrow space detection.

1. Introduction

Nature-inspired bionic robots with organism-like structures and behaviors and better adaptability in specific environments have attracted the attention of researchers in recent years. Bionic machines with different structures and functions such as bionic fish [1, 2], bionic snakes [3], bionic beavers [4], bionic caterpillars [5], other bionic robots have been developed and are widely used in rescue exploration, medical rehabilitation, military reconnaissance, industrial production, and other fields [6–10].

Bionic robots mainly include rigid robots driven by motors [11–13] and soft robots represented by flexible materials [14–17]. In terms of rigid robots driven by motors, microrobots represented by piezoelectric materials are more representative [18, 19]. In micro-robots driven by piezoelectric materials, the typical structural form is a torso and two-legged robot [20]. Jorge Hernando-Garcia designed a millimeter-sized microrobot with two piezoelectric patches attached to glass that are driven by traveling waves. The robot has a speed of up to 5 mm/s at 5 V [21]. Hariri, Hassan Hussein designed a kinematic model of a legged piezoelectric miniature robot driven by a standing wave. The robot consists of a piezoelectric bending actuator with rigidly attached legs, and the measured velocities agree well with the model predictions [22]. Due to the characteristics of piezoelectric materials, the body and foot structure of the robot are rigid materials, which have high hardness, less freedom, and are difficult to make cordless drive, and the application in some special scenarios is limited. Soft robot is a new type of robot with high structural flexibility and high degree of freedom. Soft robot is superior to traditional rigid continuum robot in adaptability and flexibility. At present, the innovation of soft robot is mainly reflected in modeling, materials, and structural design [23–25].

In nature, the inchworm has no bones in its body structure and moves with a flexed gait through the contraction and release of muscles in its body. During the movement, the trunk is transformed in an omega and linear shape. In this way, through the periodic transformation of the trunk shape, the forward movement can be achieved. This has inspired for soft crawling robots, and the imitation of inchworm crawling soft robots has become a research hotspot [26–29]. Magnetic drives are also favored by researchers in the field of bionic crawling flexible robots because of their non-contact and harmless to biological organisms [30]. Hu Wenqi designed a soft robot, established a dynamic model of the robot, studied the speed of the robot, and verified and analyzed the experimental method and theoretical model. But this robot is millimeter in size and has only a body and no other structure [31]. Sadaf introduces an asymmetric leg structure on the basis of the magnetic film, which improves the speed of movement. The force and motion mechanism of the robot are analyzed, and the feasibility of the structural design is proved. At the same time, the relationship between periodic displacement and structure size is established, and the structure design is optimized. However, the motion speed of the robot is still very slow, and the motion model only considers the displacement change of the front legs, without analyzing the whole structure [32]. In the research related to magnetically driven bionic crawling flexible robots due to the multidegree of freedom of flexible magnetically driven materials, it is more difficult to study for soft robot models.

To sum up, in the field of bionic crawling robots, the research methods of robots are different due to the different size and motion posture of robots, but the establishment of motion models is of great significance for understanding and improving soft robots. Because the materials used to manufacture soft robots are flexible, and the material properties are nonlinear, it is difficult to analyze. Soft robot has many degrees of freedom, and its motion model is difficult to establish. Therefore, the modeling and design of flexible robot is difficult. How to integrate the characteristics of flexible materials into robot modeling is a difficult problem for soft robots. After the model is established, it is difficult to solve the problem by analyzing the setting of parameters in the modeling to guide the robot manufacturing and improve the robot's motion performance.

Therefore, in terms of soft materials, we use a flexible magnetic driving film composed of NdFeb material and PDMS, as well as a robot torso composed of pI film to provide driving force for the robot. The use of pdms material does not provide wireless driving function of the robot. In terms of modeling, the principle of bionics is used to design the robot structure, analyze the robot motion posture, design the anisotropic friction structure, and establish the robot motion model. Through the model analysis, the robot optimization strategy is obtained. According to the model, by coupling the structure of the torso and legs to a flexible film, the robot can crawl under the control of a magnetic field. And the accuracy of the model is verified by experiments. Based on the motion model, the influence law of the structure size on the motion speed of the robot is obtained. The validity of the model is verified by step test experiments. Through parameter optimization, the maximum motion speed of the robot reaches 28.24 mm/s. At the same time, the robot can also move in narrow spaces such as pipes, providing the possibility of exploration in narrow spaces.

2. Materials and manufacturing methods

The unique expansion/contraction crawling method of the inchworm makes it a great advantage to maneuver in a limited space. Inspired by the movement of the inchworm, a soft-climbing robot based on magnetic field drive was designed. The design process of the robot and its driving method are introduced. According to its shape and driving mode, the motion of the soft crawling robot is introduced.

2.1. Materials

The magnetic material used in this work is an isotropic powder made of NdFeB, with an average particle size of 5 μm (MQFP-14-12-20000, Magnequench GmbH, Germany). Silicone rubber PDMS and curing agent mixed with magnetic particles were purchased from Dow Corning (Slygard 184, Mildland,

https://doi.org/10.1017/S0263574723001340 Published online by Cambridge University Press

Michigan). The material used as the trunk of the soft robot is polyimide (PI) film, and its thickness is only 0.05 mm, which has the advantages of wear resistance and tensile resistance.

2.2. Preparation of flexible magnetic film

Magnetic film actuator is a flexible film containing magnetic particles. PDMS and magnetic particles are mixed according to the mass ratio of 1: 1. The mixture was spin-coated on the glass substrate coated into PVA thins sacrificial layer (PVA 115,000, VWR) for 60 s and then solidified on the heating plate (Harry Gestigkeit GmbH) at 70°C for about 2 h. The thickness of composite films ranged from 300 to 450 μm. The next 30 s magnetization process is completed by a 2.3 T off-plane magnetic field provided by a device with two pulsed electromagnetic carburetors (EM2, Magness Corp.).

2.3. Force analysis of flexible magnetic film actuator

The magnetic field driving system is mainly composed of magnetic field generating device, control system, and driving device. The magnetic field generating device is DC24V180 kg square electromagnet, the control system is 51 microcontroller, and the driving device is L298N driver. The single chip microcomputer is used to output signals to control the alternating frequency of the magnetic field, the L298N driver is an application-specific integrated circuit, the input end can be directly connected to the single chip microcomputer, through the single chip microcomputer I/O port input signal control output voltage positive and negative, so as to control the magnetic pole direction of the square electromagnet.

For measuring the magnetic field intensity of the upper surface of the iron core, the method of equal spacing multipoint measurement is used. The spacing of each measuring point is 1 mm, and there are 12 measuring points in total. For the measurement of magnetic field strength at different heights of the upper surface, each measuring point is measured at every 1 mm elevation from the electromagnet surface in the vertical direction. Driven by 0.18 A current, the transverse and longitudinal magnetic field intensity of different measuring points on the upper surface of the iron core is measured, as shown in Fig. 1. At the same time, the magnetic field sizes of different electric currents and different heights in the middle region were measured, and origin was used for data fitting.

$$B = 58.93 \times I - 2.052 \times x + 6.37 \ (R^2 = 0.9852) \tag{1}$$

where I is the current size of square electromagnet input; x is the height of square electromagnet upper surface. The magnetic drive system is constructed and characterized. The system can control the magnetic field under voltage regulation and the size of the magnetic field can be controlled, which provides a guarantee for the robot drive.

Each magnetic particle can be regarded as an independent dipole moment. The total potential energy of magnetic membrane actuator in the magnetic field is the sum of the potential energy of magnetic moments of all these magnetic particles. The magnetic strength of a single magnetic particle can be expressed by the magnetic dipole moment, which is the sum of all the atomic dipole moment u vector in the magnetic particle:

$$m = \Sigma_{i=1}^{n} \mu_i = V \times M \tag{2}$$

Since the magnetic film is very thin, the size of the magnetic particle is far smaller than the change scale of the magnetic field, and the potential energy of $B(r_A + x) \approx B(r_A)$ in the magnetic field is

$$U(r_A) \approx -\left(\int_v M(x)\mathrm{d}^3x\right) \cdot B(r_A) = -m \cdot B(r_A) \tag{3}$$

The force of magnetic particles in magnetic field is

$$F = -\nabla U = (m \times \nabla)B = VM(\nabla B) \tag{4}$$

Suppose the total volume of magnetic material in a magnetic film is V_{total}, and because the magnetic field is perpendicular to the magnetic film, the magnetic field strength of all magnetic materials is

https://doi.org/10.1017/S0263574723001340 Published online by Cambridge University Press

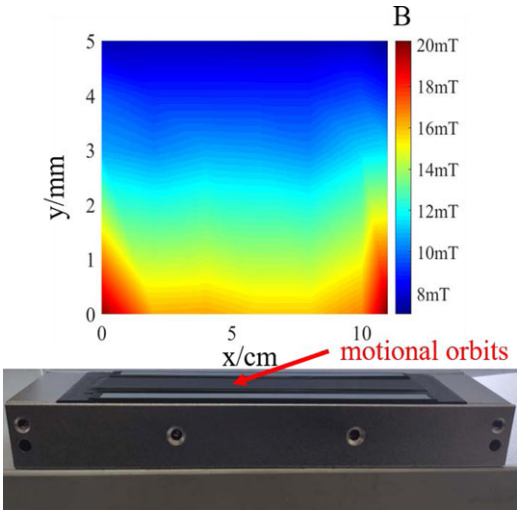

Figure 1. *Magnetic-driven system and magnetic field distribution driven by 0.18 A.*

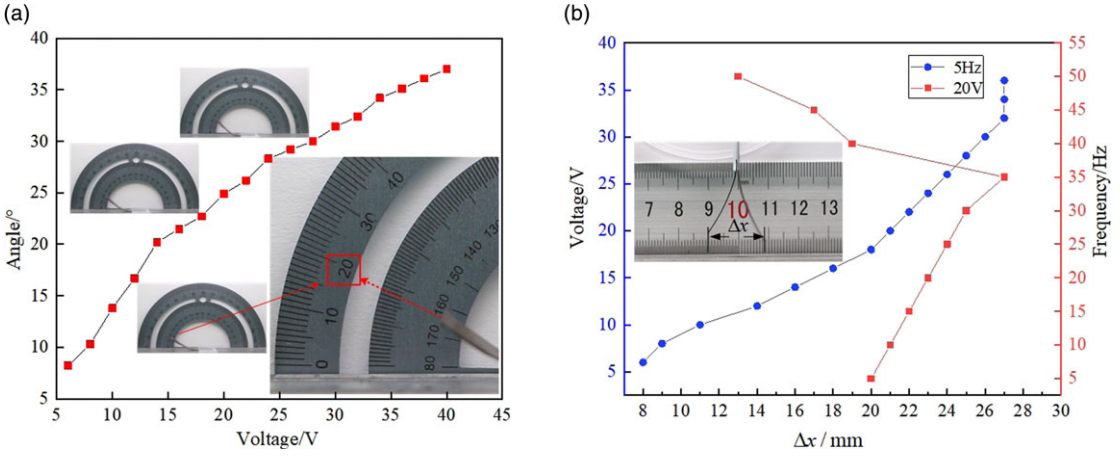

Figure 2. *Driving characteristics of flexible film (a). Angle curve under applied different voltage. (b) Displacement of the flexible film under different applied voltages and frequency.*

consistent. Therefore, the following formula is used to calculate the force and torque of a magnetic film in the external magnetic field

$$F_{\text{total}} = V_{\text{total}} M(\nabla B) \tag{5}$$

2.4. Characterization of flexible film

Samples with length of 35 mm and width of 10 mm were prepared. The deformations under alternating magnetic field and single magnetic field were tested, respectively. Place the sample on the surface of the electromagnet, with one end fixed with tape and the other end free. The magnetic field direction is set to the same magnetic field as the magnetic pole on the lower surface of the sample to generate repulsive force. A protractor is placed behind the sample to measure the bending degree. When 6 V voltage is applied to the electromagnet, the end of the sample leaves the surface of the electromagnet. As shown in Fig. 2(a), the film can complete the bending action under the effect of the magnetic field. With the increase of the magnetic field strength, the bending angle of the film also increases.

https://doi.org/10.1017/S0263574723001340 Published online by Cambridge University Press

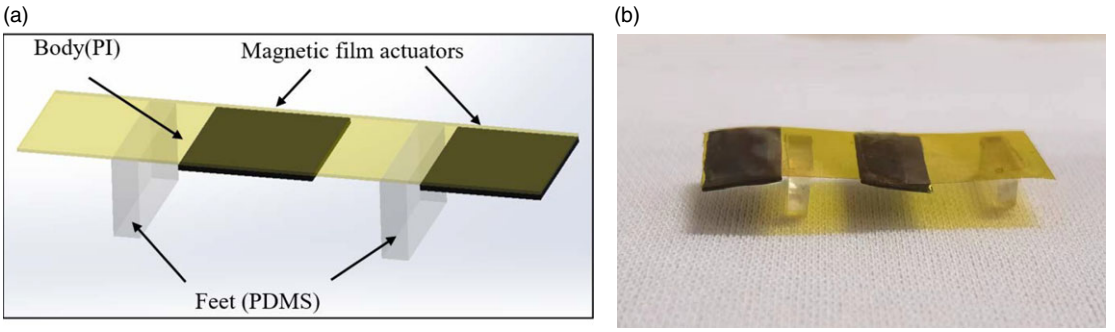

Three-dimensional structure diagram Physical image

Figure 3. *Inchworm bionic robot.*

The influence of magnetic field direction variation frequency on magnetic film deformation was studied. A 25 mm long and 10 mm wide sample was prepared with one end fixed vertically above the electromagnet and the other end free. A digital camera was used to record the displacement of the sample under the magnetic field changing in the direction of the magnetic field. The test results are shown in Fig. 2(b). At a fixed frequency of 5 Hz, the displacement of the sample increases with the increase of voltage. When the voltage reaches 32 V, the displacement reaches the maximum of 27 mm. In the case of a fixed voltage of 20 V, the displacement increases with the increase of frequency in the range of 5–35 Hz and reaches the maximum displacement when it reaches 35 Hz. If the magnetic field change frequency continues to increase, the displacement will suddenly decrease, and it is smaller than the displacement at 5 Hz. This is because after the frequency is increased, the response time of the magnetic film will be reduced, so the displacement becomes smaller. Therefore, the magnetic film is affected by the size of the magnetic field and the frequency of magnetic field change, which can be combined with the crawling action of the robot to produce different crawling speed.

2.5. Robot design

Inspired by the movement mode of inchworm, a magnetically driven flexible crawling robot was designed according to the characteristics of flexible magnetic film. The structure is shown in Fig. 3. The flexible robot mainly consists of a torso and foot structure that mimic the body of an inchworm, where the main structure of the torso is a PI film (polyimide film) and two flexible magnetic films with opposite magnetic properties, and the foot structure consists of two rectangular structures of PDMS material. The torso part provides the driving force, and the foot structure supports the whole body and provides the grip. The flexible magnetic film acts as an actuator to control the expansion and contraction of the entire body. The different force directions of the two magnetic films make the structure switch back and forth between “concave” and “arch bridge” and then realize the crawling action.

In the structural design, the overall structure of the robot is π-shaped, and the foot structures are located under the left and right sides of the torso. The front and rear foot structures of the robot are the same, but for the bionic crawling behavior of the robot, the front and rear feet are required to provide different friction forces. The drive unit is two magnetically opposite drive films that generate forces in opposite directions when subjected to a magnetic field. Using these two differently directed forces, they act on the foot structure through the torso, causing the foot structure to generate different pressures on the ground. Therefore, one of the foot structures needs to be subjected to the force in the opposite direction of the two magnetic membranes, and the other foot structure needs to be subjected to the force generated by only one magnetic membrane. In this way, the forces on the two feet structures are made to be different in order to change the friction of the robot in different motion postures. Thus, the position of the magnetic film is not symmetrical on the torso of the robot, which in turn determines the relative position of the magnetic film on the torso, where one flexible magnetic film actuator is located on the

https://doi.org/10.1017/S0263574723001340 Published online by Cambridge University Press

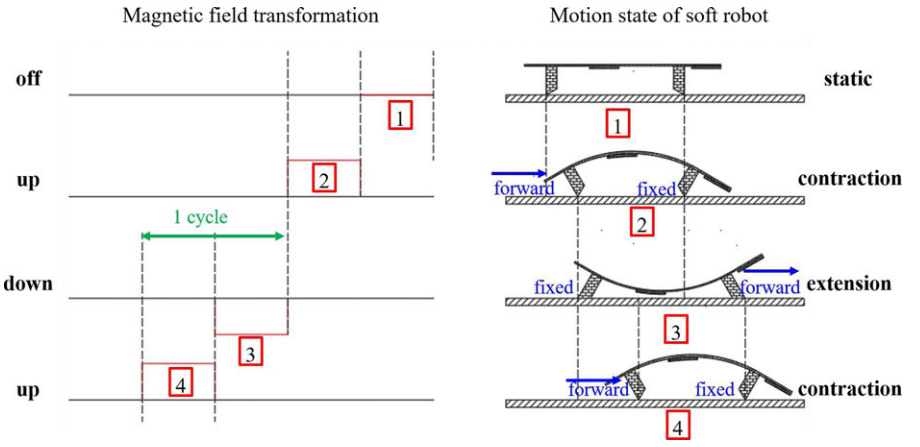

Figure 4. *Time-dependent magnetic field and corresponding motion of the soft robot. The magnetic field is sequentially applied on the soft robot in up-and-down manner.*

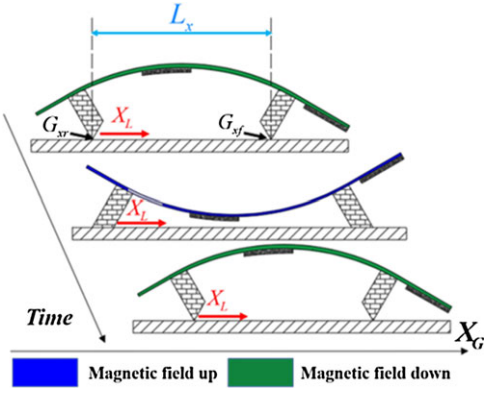

Figure 5. *Schematic diagram of the forces acting on the soft robot.*

anterior side of the foot structure and the other flexible actuator is located in the middle of the two feet structures.

3. Modeling of the soft crawling robot

3.1. Crawing mechanism analysis

According to the above model and the force analysis of the magnetic film under the magnetic field, the crawling mechanism of the robot is obtained. When there is no magnetic field driving, the magnetic film is not stressed, the two legs are used as support, and the soft robot is stationary. During the first half of the cycle, when the applied magnetic field is upward, the head is pressed down, the belly arches, the front legs are anchored, and the entire body shrinks into an open downward arc, which causes the back legs to slide one step forward. In the second half cycle, the magnetic field is directed downward, the head is raised, the belly is pressed down, the hind legs are imbibed, the robot is extended in an open upward arc, and the front legs slide forward. So the whole robot is crawling forward, cycle by cycle. Of course, when the initial magnetic field is applied downward, the structure stretches and then contracts and can also move forward. Figure 4 shows the magnetic field changing over time and the corresponding motion of the soft robot in one motion period.

In order to explain how the deformation of the robot's body affects the robot's motion, the worm-like kinematics is studied. Assume that the leg as the fixed end does not slip, the crawling process is shown in Fig. 5. Because the soft-footed worm robot can move in one dimension, it does not need to consider the

https://doi.org/10.1017/S0263574723001340 Published online by Cambridge University Press

direction of movement. Taking the forward direction of the soft robot as the positive direction, a global coordinate system is established to represent the position of the two legs of the robot (leg thickness is ignored). The positions of the front and rear legs with respect to the global coordinate system are, respectively, G_{xf} and G_{xr}, and the length between the legs $L_x = G_{xf} - G_{xr}$, then $\frac{dL_x}{dt} = \frac{dG_{xf}}{dt} - \frac{dG_{xr}}{dt}$. $\frac{dL_x}{dt}$ represents the two motion stages of a soft robot. If it is less than zero, the front legs are fixed, the back legs are brought forward, and the body is contracted. If greater than zero, the back legs are fixed, the front legs are brought forward, and the body is extended. According to the assumption, there is

$$\frac{dL_x}{dt} = \begin{cases} -\frac{dG_{xr}}{dt}, \frac{dL_x}{dt} < 0 \\ \frac{dG_{xf}}{dt}, \frac{dL_x}{dt} > 0 \end{cases} \tag{6}$$

Through integral calculation with the time product, the total displacement of the front foot and the back foot in different periods relative to the global coordinate system can be written as

$$G_{sr} = \begin{cases} \sum_{i=0}^{n} \int_0^t -\frac{dGxr}{dt} d\tau, T \times n \le \frac{T}{2} \times (2n+1) \\ 0, T \times (2n+1) \le t \le T \times (2n+2) \end{cases} \tag{7}$$

$$G_{sf} = \begin{cases} 0, T \times n \le t \frac{T}{2} \times (2n+1) \\ \sum_{i=0}^{n} \int_0^t -\frac{dGxr}{dt} d\tau, T \times (2n+1) \le t \le T \times (2n+2) \end{cases} \tag{8}$$

Equation (7) represents the sum of motion displacement values of the first half cycle of the hind leg in different cycles, and Eq. (8) represents the sum of motion displacement values of the second half cycle of the front leg in different cycles. The displacement value of the software intelligent structure in several cycles can be expressed by G_{sf} or G_{sr}, since the robot's motion is holistic, then $G_{sr} \approx G_{sf}$. Therefore, the average velocity of the software intelligent structure can be defined as

$$G_{\bar{v}t} = \frac{1}{2t} \int_0^t \left| \frac{dL_x}{dt} \right| d\tau \tag{9}$$

According to the above analysis, if the change of L_x is given, the motion speed of the robot can be determined. Therefore, the motion model of the soft crawling robot is established based on its motion attitude.

3.2. Motion model based on static beam bending analysis

The posture of the soft crawling robot is similar to an arch bridge, so it is modeled as an arc. The modeling analysis of the soft crawling robot is shown in Fig. 6. Assume that the torso of the soft robot is bent into a regular arc. During the movement, the fixed support end determined by the force analysis does not slip and move backward. Under these assumptions, the forward distance of the soft robot in a period is calculated, and then the speed of the soft robot is calculated.

When the soft crawling robot is stationary, the distance between the legs is L. When the upward magnetic field is generated, the trunk of the soft crawling robot arches upward. The angle between the front and rear legs and the vertical direction is θ_1 and θ_2, respectively. The legs extend to form a fan with the trunk, with a radius of R_1 and an angle of θ. The distance x_1 between the front and rear legs on the contact surface is shown in Eq. (10).

$$x_1 = \left(\frac{180 \times l}{\theta \times \pi} - H \right) \times (\sin\theta_1 + \sin\theta_2) \tag{10}$$

https://doi.org/10.1017/S0263574723001340 Published online by Cambridge University Press

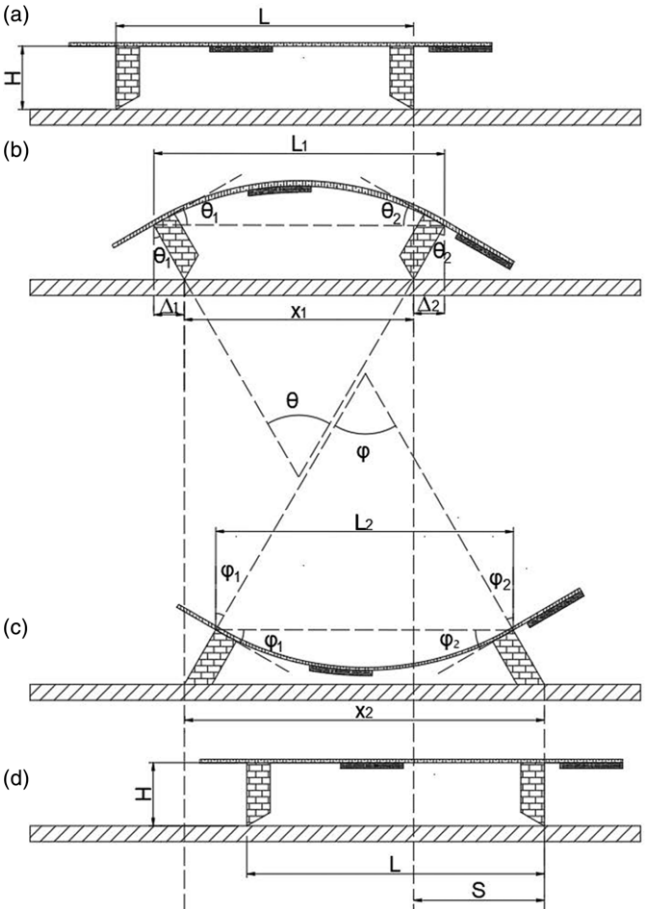

Figure 6. *Modeling analysis of soft crawling robot.*

where H represents the height of soft robot's leg; L_1 represents the distance between the legs of the trunk when the structure arches. x_1 represents the distance between the legs of the contact surface when the structure is arched.

When the magnetic field direction is reversed, soft crawling robot from arching state to downward concave. The angle between the front and rear legs and the vertical direction is φ_2 and φ_1, respectively. The legs extend to form a fan with the trunk, with a radius of R_2 and an angle of φ. The distance x_2 between the front and rear legs on the contact surface is shown in Eq. (11).

$$x_2 = \left(\frac{180 \times l}{\varphi \times \pi}\right) \times (\sin\varphi_1 + \sin\varphi_2) \tag{11}$$

where L_2 represents the distance between the legs of the trunk when the structure concaves. x_2 represents the distance between the legs of the contact surface when the structure is concaved.

The process from (a) to (d) in Fig. 5 is exactly a cycle. Based on the front leg, the forward distance of the front leg is the displacement of the soft crawling robot in one cycle. More specifically, s can be expressed as

$$s = x_2 - x_1 \tag{12}$$

The motion time of a period from (a) to (d) is also the change time of an alternating magnetic field, and the alternating frequency of the magnetic field is f. Assuming that the displacement of the soft-climbing

https://doi.org/10.1017/S0263574723001340 Published online by Cambridge University Press

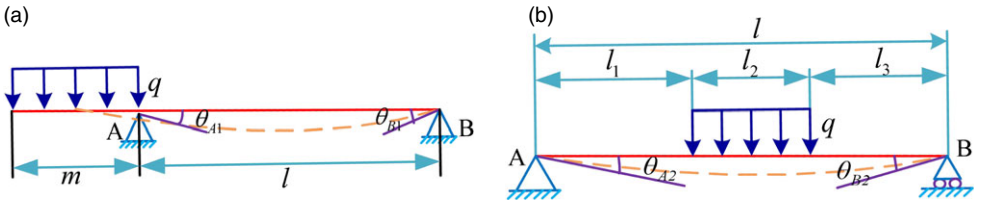

The uniform load on the head. The uniform load on the abdomen.

Figure 7. *Simply supported beam structure.*

robot in each cycle is equal, the moving speed v of the soft robot can be approximated as the product of the moving distance s of each cycle and the f frequency of magnetic field change:

$$v = s \times f \tag{13}$$

According to the formula, when the displacement of each step is determined, the faster the magnetic field change frequency, the greater the motion speed of the software intelligent structure.

In order to determine the bending angle of the dynamic model, the bending condition of the body was analyzed mechanically. The whole soft crawling robot was regarded as a beam structure, and the magnetic field force received by the magnetic film in the uniform magnetic field was regarded as the uniform distribution load. When the bending angle generated by the uniform load on the head is calculated, the robot is regarded as an overstretched simply supported beam structure, as shown in Fig. 7(a); when the bending angle generated by the uniform load on the abdomen is calculated, the robot is regarded as a simply supported beam structure, as shown in Fig. 7(b). The sum of angles produced by the force of the head and abdomen is the change in the angle of the concave or arched legs of the intelligent structure.

From the angle formula of the extended beam, the angles of A and B in Fig. 7(a) are

$$\theta_{A1} = \frac{qm^2 l}{6EI}, \quad \theta_{b1} = \frac{qm^3 l}{12EI} \tag{14}$$

where l represents the distance between legs; m represents the Length of head magnetic film; E represents the Young's modulus of trunk material; I represents the moment of inertia of the trunk; and q represents the load force on magnetic film. The length and width of the trunk are, respectively, b and h. The formula of the moment of inertia is

$$I = \frac{bh_3}{12} \tag{15}$$

where b represents the width of the trunk; h represents the thickness of trunk.

$$q = \frac{F_{\text{total}}}{m \times b} \tag{16}$$

where F_{total} represents total force on the magnetic film; b represents the width of magnetic film.

From the angle formula of the simply supported beam structure, the angles of A and B in Fig. 7(b) are

$$\begin{aligned} \theta_{A2} &= \frac{ql_3}{6EIl}\left(l_2 + \frac{l_3}{2}\right) \times \left[\left(l_1 + \frac{l_3}{2}\right) \times \left(l + l_2 + \frac{l_3}{2}\right) - \frac{1}{4}l_3^2\right] \\ \theta_{B2} &= \frac{ql_3}{6EIl}\left(l_1 + \frac{l_3}{2}\right) \times \left[\left(l_2 + \frac{l_3}{2}\right) \times \left(l + l_1 + \frac{l_3}{2}\right) - \frac{1}{4}l_3^2\right] \end{aligned} \tag{17}$$

where θ_{A2} represents the angle change of fixed hinge support end; θ_{B2} represents the angle change of roller bearing end; l_1 represents the displacement from uniform load boundary to fixed hinge support; l_2 represents the transverse size of the abdominal magnetic film; l_3 represents the displacement from uniform load boundary to roller bearing; and l represents the distance between legs, $l = l_1 + l_2 + l_3$.

https://doi.org/10.1017/S0263574723001340 Published online by Cambridge University Press

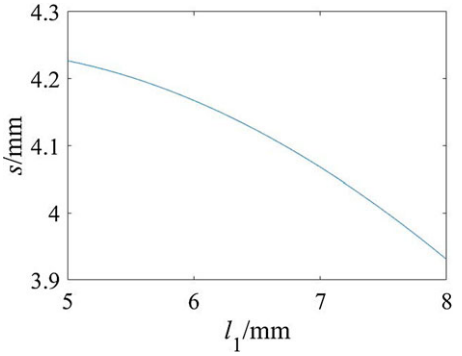

Figure 8. *The relationship between the distance l_1 between the two magnetic films and the displacement s of each step.*

When the body arches upward, the front leg is fixed and the rear leg can move. At this time, the bending angle of the front and rear legs is

$$\begin{aligned} \theta_2 &= \theta_{A1} + \theta_{A2} \\ \theta_1 &= \theta_{B1} + \theta_{B2} \end{aligned} \tag{18}$$

When the body concaves upward, the rear leg is fixed and the front leg can move. And the bending angle of the front leg is the angle of the roller shaft support. However, the positions of the two support ends have been interchanged, and the positions of l_1 and l_3 have also been reversed, so at this time the angles of A and B are changed to:

$$\begin{aligned} \theta_{A2} &= \frac{ql_1}{6EIl}\left(l_3 + \frac{l_1}{2}\right) \times \left[\left(l_2 + \frac{l_1}{2}\right) \times \left(l + l_3 + \frac{l_1}{2}\right) - \frac{1}{4}l_1^2\right] \\ \theta_{B2} &= \frac{ql_1}{6EIl}\left(l_2 + \frac{l_1}{2}\right) \times \left[\left(l_3 + \frac{l_1}{2}\right) \times \left(l + l_2 + \frac{l_1}{2}\right) - \frac{1}{4}l_1^2\right] \end{aligned} \tag{19}$$

where θ_{A2} represents the angle change of roller bearing end. θ_{B2} represents the angle change of the fixed hinge support end.

The bending angles of the front and rear legs are

$$\begin{aligned} \varphi_2 &= \theta_{A1} + \theta_{A2} \\ \varphi_1 &= \theta_{B1} + \theta_{B2} \end{aligned} \tag{20}$$

The simulation results are calculated by MATLAB to determine the relationship between structural size and periodic motion displacement. It can be seen from the above dynamic model of the soft robot that the size of s is determined by many variables, so this paper uses a single variable to calculate.

From the formula, when the other parameters except H are determined, the longer the leg, the greater the displacement of each step. Therefore, the influence of leg length on motion speed can be determined as positive correlation. Except for the leg length, only the parameters l_1 and l are not fixed, and the parameters of these fixed values: $m = 8.5$ mm, $E = 115$ MPa, $b = 10$ mm, $h = 0.4$ mm, $H = 5$ mm, $l_2 = 10.5$ mm, and $q = 5\ \mathrm{N/m^2}$.

When $l = 21$ mm, MATLAB is used to simulate the relationship between the distance l_1 from the abdominal magnetic film to the front leg and the displacement s of each step. The results are shown in Fig. 8. The figure shows that with the increase of the distance from the abdominal magnetic film to the front leg, the motion displacement of each step decreases gradually. In fact, the distance between the two magnetic films becomes smaller with the gradual reduction. But the force of the structure will be too concentrated to produce relative sliding.

When $l_1 = 6.5$ mm, MATLAB is used to simulate the relationship between the distance l from the abdominal magnetic film to the front leg and the displacement s of each step. The results are shown in

https://doi.org/10.1017/S0263574723001340 Published online by Cambridge University Press

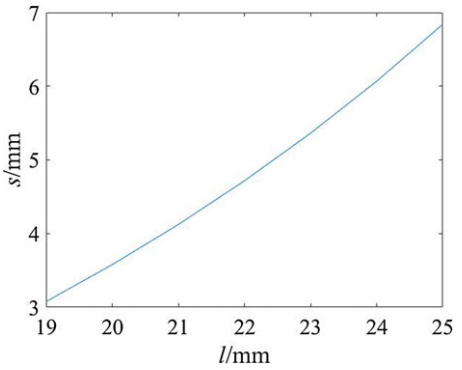

Figure 9. *The relationship between the distance l between the two legs and the displacement s of each step.*

Fig. 9. The figure shows that with the larger the distance between the legs, the greater the displacement of each step. However, the distance between the legs cannot be infinitely increased proceed from actual conditions; otherwise, it will lead to the disappearance of structural balance.

After simulation, it is concluded that with the increase of the distance from the abdominal magnetic film to the front leg, the movement displacement of each step gradually decreases. The greater the distance between the legs, the greater the movement tendency of each step. Therefore, in practical design, it provides theoretical support for determining the size of each part of the robot. The simulation results of the motion model provide theoretical support for the structural design of the robot. Although the factors of the motion model are not comprehensive, some states of the model are ideal, and there are certain differences with the reality. But it still provides a reference for robot optimization.

4. Experiment of robot crawling

4.1. Validation of the model

The actual size of the robot is brought into the dynamic model and compared with the data obtained from the experimental study to verify the correctness of the model. The research object is a soft crawling robot with 4.24 mm leg length and 23 mm spacing. The driving parameters of the magnetic field are 24 V voltage and 10 Hz frequency. Randomly selected from the same motion process of four motion cycles, four periodic structure of the motion posture as shown in Fig. 10, by measuring the movement distance between the legs as shown in Table I.

In Table I, $x_2 - x_1$ is the theoretical value derived by the formula, and s is the actual value measured. It can be seen from Table I that the model-predicted value of the distance between the two legs is very close to the experiment result, which proves the correctness of the theoretical modeling. According to Experiment result 4 in Table I, the actual motion distance is far less than the theoretical value. It can be seen from Fig. 10 that the front leg does not remain fixed in the process of arching but slips backward. Especially, the distance of the experiment result 4 slips backward is the largest, about 3 mm, which leads to a small actual step.

From the above analysis, the model is basically consistent with the actual situation. However, the error caused by the slip of the leg makes some theoretical values differ greatly from the actual values. which affects the actual speed of the soft robot.

4.2. Experiment of movement speed

To explore the motion law of soft robot with different structure sizes. Five soft robots of different sizes were selected for velocity measurement experiments under different magnetic fields. Five kinds of size

https://doi.org/10.1017/S0263574723001340 Published online by Cambridge University Press

Table I. *The experiment result and theoretical value of the distance between the two legs of inchworm.*

	x_2/mm	x_1/mm	$x_2 - x_1$/mm	s/mm
Model-predicted value	24.9	20.3	4.6	4.6
Experiment result 1	25.4	20.4	5.0	4.3
Experiment result 2	26.0	20.7	5.3	4.2
Experiment result 3	26.0	20.5	5.5	4.7
Experiment result 4	26.2	21.7	4.5	1.0

Table II. *Structural dimensions of five soft robots.*

Type	Leg length/mm	Distance between legs/mm
Type 1	4	22
Type 2	5	24
Type 3	3	21
Type 4	4	24
Type 5	5	23

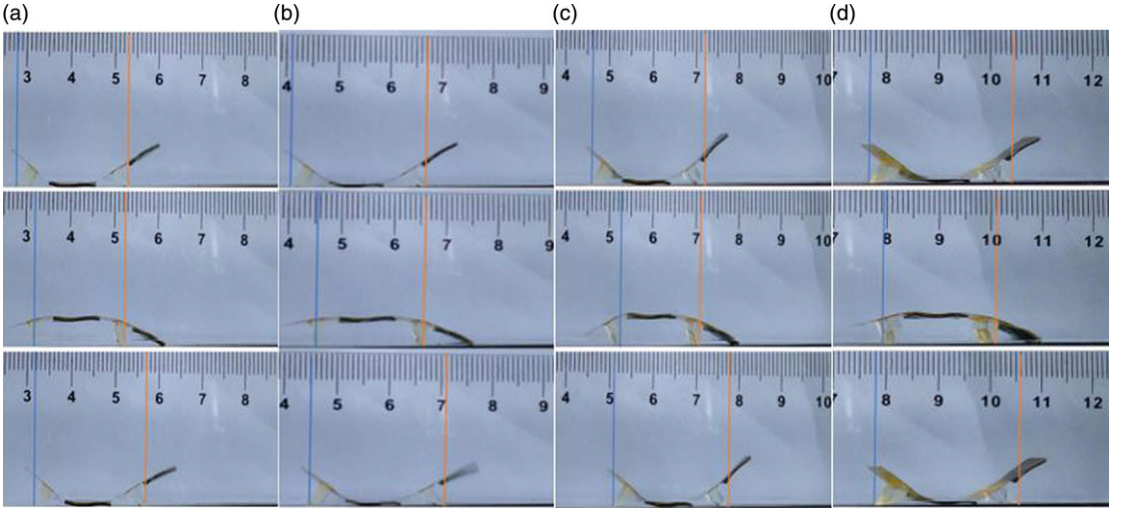

Figure 10. *Displacement diagram of robot at different time.*

soft robots, as shown in Table II, measure the magnetic field velocity of five kinds of soft robots under different intensity and different frequency.

Five types of soft robot are driven under magnetic field, 10 mT magnetic field, and the corresponding velocities under different magnetic field change frequencies are shown in Fig. 11. Figure 11(a) shows the actual curve of motion velocity, and Fig. 11(b) shows the fitting curve of motion velocity.

In Fig. 11, we know from curves 2 and 4, when the distance is fixed, the longer the leg, the faster the movement speed. It can be seen from curves 1 and 4 that when the leg length is constant, the greater the distance, the faster the motion speed. The Type 5 software intelligent structure has the longest legs and the spacing is not the largest, but its movement speed is the fastest. This shows that the distance between the two legs cannot be increased indefinitely, otherwise it will affect the speed of movement of the intelligent structure. Of course, the longer the leg is not the bigger the better, too long the leg not only increases the weight of the intelligent structure but also makes the center of gravity too high, reducing the stability of the movement.

https://doi.org/10.1017/S0263574723001340 Published online by Cambridge University Press

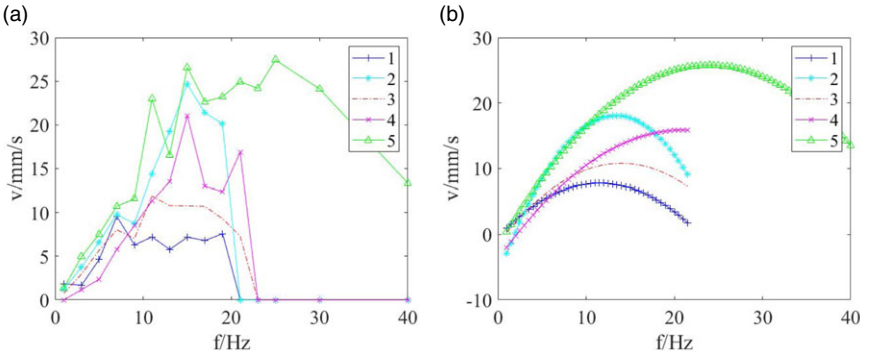

Actual crawing speed Curve crawing speed

Figure 11. *The curve of velocity versus frequency of five soft robots with different sizes.*

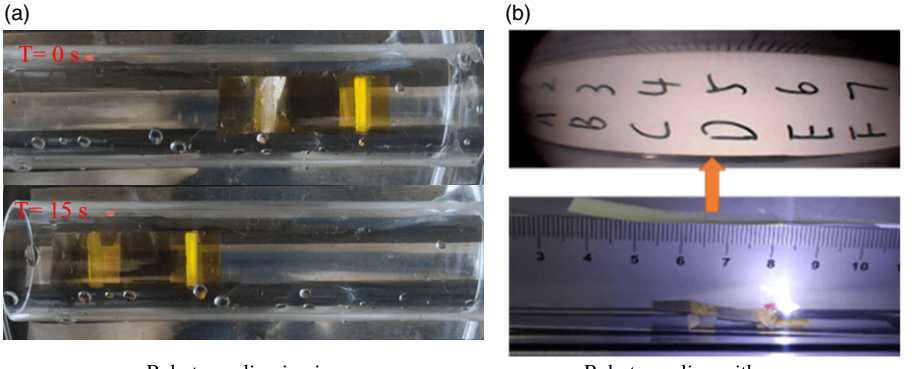

Robot crawling in pipe Robot crawling with camera

Figure 12. *Exhibition of robot crawling.*

As can be seen from Fig. 11, the effects of robot size and voltage frequency on robot crawling speed are obtained through simulation. Because the model does not consider gravity and other factors, the actual speed and the theoretical speed have a certain difference, but the overall trend is consistent, which also provides a reference for the choice of robot drive parameters and robot size. Through theoretical analysis, it is concluded that the robot with Type 5 can get the maximum motion speed under the magnetic field with frequency of 25 Hz, and in the actual experiment, the robot with size 5 can also get the maximum speed of 28.24 mm/s under the magnetic field of 25 Hz (Supplementary video 1).

4.3. Exercise effect under different external environment

The robot was placed in the pipe to crawl, mainly simulating the industrial pipe environment with small aperture. The pipe chosen in this experiment was a transparent rubber tube with an internal space diameter of 12 mm. The pipe was fixed above the moving track and the robot's moving speed was recorded. As shown in Fig. 12(a), the robot's maximum motion speed in the pipeline is 13.78 mm/s, which is slower than that in flat ground (supplementary video 2). The main reason is that only the edges of its legs contact the inner wall of the pipeline, and the contact surface is too small.

The endoscope lens is mounted on the torso of the robot's hind leg, with the lens facing upwards. The upper torso of the hind leg is equipped with a camera, which can be used to observe the actual situation on the upper wall of the pipeline (supplementary video 3). The observation effect is shown in Fig. 12(b). In this case, the effect of line arrangement on motion is minimal.

https://doi.org/10.1017/S0263574723001340 Published online by Cambridge University Press

5. Conclusion

Based on the motion of inchworm, a soft crawling robot driven by magnetic field was designed. On the basis of magnetic field control, a motion model based on motion attitude is established. By analyzing the size and force of the soft robot, the periodic displacement and velocity of the robot are determined and the optimization parameters of the soft robot design are obtained. The motion velocity given by the motion model is different from the actual velocity of the robot. The reason for these differences is that the model is built under ideal conditions, while the friction force will cause the deviation of the robot's leg displacement in the actual movement. However, the modeling process still provides research ideas for the optimization of soft robot, and the optimization of leg structure becomes the key to our next work. In addition, the robot can move in small spaces such as pipes and carry endoscopes, which provides the possibility for exploration in small spaces.

Author contributions. Yuyan Zhang and Yintang Wen conceived and designed the study. Yue Di performed experiment analyses. Yaxue Ren wrote the article.

Financial support. This work was supported by the S&T Program of Hebei (grant no. 216Z1704G).

Competing interests. The authors declare no competing interests exist.

Ethical approval. Not applicable.

Supplementary material. The supplementary material for this article can be found at https://doi.org/10.1017/S0263574723001340

References

[1] G. Chen, X. Yang, Y. D. Xu, Y. W. Lu and H. S. Hu, "Neural network-based motion modeling and control of water-actuated soft robotic fish," *Smart Mater. Struct.* **32**(1), 015004 (2023).
[2] G. Chen, Z. Zhao, Z. Wang, J. Tu and H. Hu, "Swimming modeling and performance optimization of a fish-inspired underwater vehicle (FIUV)," *Ocean Eng.* **271**, 113748 (2023).
[3] M. J. Koopaee, S. Bal, C. Pretty and X. Q. Chen, "Design and development of a wheel-less snake robot with active stiffness control for adaptive pedal wave locomotion," *J. Bionic Eng.* **16**(4), 593–607 (2019).
[4] G. Chen, W. Peng, Z. Wang, J. Tu, H. Hu, D. Wang, H. Cheng and L. Zhu, "Modeling of swimming posture dynamics for a beaver-like robot," *Ocean Eng.* **279**, 114550 (2023).
[5] C.-W. Song, D.-J. Lee and S.-Y. Lee, "Bioinspired segment robot with earthworm-like plane locomotion," *J. Bionic Eng.* **13**(2), 292–302 (2016).
[6] M. W. Han, M. S. Kim and S. H. Ahn, "Shape memory textile composites with multi-mode actuations for soft morphing skins," *Compos. B Eng.* **198**, 108170 (2020).
[7] S. Jeon, S. Kim, S. Ha, S. Lee, E. Kim, S. Y. Kim, S. H. Park, J. H. Jeon, S. W. Kim, C. Moon, B. J. Nelson, J. Y. Kim, S. W. Yu and H. Choi, "Magnetically actuated microrobots as a platform for stem cell transplantation," *Sci. Robot.* **4**(30), eaav4317 (2019).
[8] S. Palagi, A. G. Mark, S. Y. Reigh, K. Melde, T. Qiu, H. Zeng, C. Parmeggiani, D. Martella, A. Sanchez-Castillo, N. Kapernaum, F. Giesselmann, D. S. Wiersma, E. Lauga and P. Fischer, "Structured light enables biomimetic swimming and versatile locomotion of photoresponsive soft microrobots," *Nat. Mater.* **15**(6), 647– (2016).
[9] Z. W. Shao, L. T. Yu and J. Li, "A Method for Self-Service Rehabilitation Training of Human Lower Limbs," **In:** *15th IEEE International Conference on Automation Science and Engineering (IEEE CASE)* (2019) pp. 158–163.
[10] L. Wang, H. K. Bisoyi, Z. G. Zheng, K. G. Gutierrez-Cuevas, G. Singh, S. Kumar, T. J. Bunning and Q. Li, "Stimuli-directed self-organized chiral superstructures for adaptive windows enabled by mesogen-functionalized graphene," *Mater. Today* **20**(5), 230–237 (2017).
[11] H. B. Zang, D. F. Zhao and L. G. Shen, "Theoretical study of global scale analysis method for agile bionic leg mechanism," *Robotica* **38**(3), 427–441 (2020).
[12] A. J. Ijspeert, "Biorobotics: Using robots to emulate and investigate agile locomotion," *Science* **346**(6206), 196–203 (2014).
[13] K. Ren and J. C. Yu, "Research status of bionic amphibious robots: A review," *Ocean Eng.* **227**, 108862 (2021).
[14] J. Z. Fan, S. Q. Wang, Y. Wang, G. Li, J. Zhao and G. F. Liu, "Research on frog-inspired swimming robot driven by pneumatic muscles," *Robotica* **40**(5), 1527–1537 (2022).
[15] R. Q. Wang, C. Zhang, Y. W. Zhang, W. J. Tan, W. Y. Chen and L. Q. Liu, "Soft underwater swimming robots based on artificial muscle," *Adv. Mater. Technol.* **8**(4), 2200962 (2023).

[16] Q. F. Han, A. H. Ji, N. Jiang, J. Hu and S. N. Gorb, "A climbing robot with paired claws inspired by gecko locomotion," *Robotica* **40**(10), 3686–3698 (2022).
[17] Z. Y. Liu, Y. X. Wang, J. B. Wang, Y. Q. Fei and Q. T. Du, "An obstacle-avoiding and stiffness-tunable modular bionic soft robot," *Robotica* **40**(8), 2651–3665 (2022).
[18] J. Li, J. Deng, S. Zhang and Y. Liu, "Development of a miniature quadrupedal piezoelectric robot combining fast speed and nano-resolution," *Int. J. Mech. Sci.* **250**, 108276 (2023).
[19] S. A. Rios, A. J. Fleming and Y. K. Yong, "Miniature resonant ambulatory robot," *IEEE Robot. Autom. Lett.* **2**(1), 337–343 (2017).
[20] A. G. Dharmawan, H. H. Hariri, G. S. Soh, S. Foong and K. L. Wood, "Design, analysis, and characterization of a two-legged miniature robot with piezoelectric-driven four-bar linkage," *J. Mech. Robot.* **10**(2), 021003 (2018).
[21] J. Hernando-Garcia, J. L. Garcia-Caraballo, V. Ruiz-Diez and J. L. Sanchez-Rojas, "Motion of a legged bidirectional miniature piezoelectric robot based on traveling wave generation," *Micromachines* **11**(3), 321 (2020).
[22] H. Hariri, Y. Bernard and A. Razek, "Dual piezoelectric beam robot: The effect of piezoelectric patches' positions," *J. Intel. Mater. Syst. Struct.* **26**(18), 2577–2590 (2015).
[23] J. Bishop-Moser and S. Kota, "Design and modeling of generalized fiber-reinforced pneumatic soft actuators," *IEEE Trans. Robot.* **31**(3), 536–545 (2015).
[24] D. Rus and M. T. Tolley, "Design, fabrication and control of soft robots," *Nature* **521**(7553), 467–475 (2015).
[25] G. Wang, D. Chen, K. Chen and Z. Zhang, "The current research status and development strategy on biomimetic robot," *J. Mech. Eng.* **51**(13), 27–44 (2015).
[26] J. W. Cao, W. Y. Liang, Y. Z. Wang, H. P. Lee, J. Zhu and Q. Y. Ren, "Control of a soft inchworm robot with environment adaptation," *IEEE Trans. Ind. Electron.* **67**(5), 3809–3818 (2020).
[27] H. Q. Niu, R. Y. Feng, Y. W. Xie, B. W. Jiang, Y. Z. Sheng, Y. Yu, H. X. Baoyin and X. Y. Zeng, "Magworm: A biomimetic magnet embedded worm-like soft robot," *Soft Robot.* **8**(5), 507–518 (2021).
[28] J. A. Steiner, L. N. Pham, J. J. Abbott and K. K. Leang, "Modeling and analysis of a soft endoluminal inchworm robot propelled by a rotating magnetic dipole field," *J. Mech. Robot.* **14**(5), 051002 (2022).
[29] C. Wang, H. Z. Li, Z. Z. Zhang, P. F. Yu, L. H. Yang, J. L. Du, Y. Niu and J. Jiang, "Review of bionic crawling micro-robots," *J. Intell. Robot. Syst.* **105**(3), 56 (2022).
[30] B. L. Gray, "A review of magnetic composite polymers applied to microfluidic devices," *J Electrochem. Soc.* **161**(2), B3173–B3183 (2014).
[31] W. Hu, G. Z. Lum, M. Mastrangeli and M. Sitti, "Small-scale soft-bodied robot with multimodal locomotion," *Nature* **554**(7690), 81–85 (2018).
[32] S. Ijaz, H. Li, M. C. Hoang, C.-S. Kim, D. Bang, E. Choi and J.-O. Park, "Magnetically actuated miniature walking soft robot based on chained magnetic microparticles-embedded elastomer," *Sens. Actuators A Phys.* **301**, 111707 (2020).

Cite this article: Y. Di, Y. Zhang, Y. Wen and Y. Ren (2024). "Modeling and optimization of motion for inchworm-inspired magnetically driven soft robot", Robotica **42**, 72–86. https://doi.org/10.1017/S0263574723001340